Article

Changes in Structural, Morphological and Optical Features of Differently Synthetized C_3N_4-ZnO Heterostructures: An Experimental Approach

Arianna Actis [1], Francesca Sacchi [1], Christos Takidis [1], Maria Cristina Paganini [1,*] and Erik Cerrato [2]

1   Department of Chemistry and NIS, University of Torino, Via P. Giuria 7, 10125 Torino, Italy
2   NRIM Istituto Nazionale di Ricerca Metrologica, I-10135 Torino, Italy
*   Correspondence: mariacristina.paganini@unito.it

Abstract: C_3N_4 is an innovative material that has had huge success as a photocatalyst in recent years. More recently, it has been coupled to robust metal oxides to obtain more stable materials. This work is focused on the different synthesis techniques used to prepare bare C_3N_4 and combined C_3N_4/ZnO mixed systems. Different precursors, such as pure melamine and cyanuric acid-based supramolecular complexes, were employed for the preparation of the C_3N_4 material. Moreover, different solvents were also used, demonstrating that the use of water leads to the formation of a more stable heterojunction. Structural (XRD), morphological (FESEM) and optical (UV-vis) measurements underlined the role of the precursors used in the preparation of the materials. A clear trend can be extrapolated from this experimental approach involving different intimate contacts between the two C_3N_4 and ZnO phases, strictly connected to the particular preparation method adopted. The use of the supramolecular complexes for the preparation of C_3N_4 leads to a tighter association between the two phases at the heterojunction, resulting in much higher visible light harvesting (connected to lower band gap values).

Keywords: C_3N_4; ZnO; heterojunction; photocatalyst

1. Introduction

The search for new photoactive materials working in the visible frequency range of the solar spectrum is one of the most interesting and urgent challenges that the scientific community has to face. Among all of the possible candidates, C_3N_4-based materials have played a prominent role since the beginning of the century. The classic photocatalytic process is based on the exploitation of light energy, possibly falling into visible solar frequencies, to promote chemical transformations [1–3]. Photocatalytic reactions are employed for many purposes: from the decontamination of pollutants in wastewater [4,5] to the generation of fuels from the water photo-splitting reaction (producing H_2) [6,7] and the photo-reduction of CO_2 to generate useful chemical compounds (i.e., usually methanol) [8,9]. All of these processes aim to reduce the environmental impact caused by humans through the contamination and consumption of the planet's resources [10,11]. Recent studies demonstrated that the most suitable systems are semiconductor metal oxides thanks to their robustness, stability and availability. Their intrinsic band structure allows them to induce the promotion of electrons into the conduction band (CB), leaving holes in the valence band (VB) when an appropriate amount of energy, equal to or higher than the band gap width, is applied to the material [2]. Once at the semiconductor surface, the photo-generated charge carriers, i.e., electrons and holes, can facilitate reductive (H_2 photo-production and CO_2 photo-reduction) and oxidative (photo-degradation) redox reactions, respectively. The band gap of the materials, their surface area and their crystallinity are paramount parameters in determining photoactivity. In many cases, the most stable and widely used materials (i.e., TiO_2) present a high band gap, much higher than visible light wavelengths. To overcome

this inconvenience, two main strategies are followed: the doping of materials and the formation of heterojunctions. The doping procedure has been widely described in the past, while the use of heterojunctions is still under debate. The formation of heterojunctions at material interfaces occurs in the band alignment; the best performance of this technology has turned out to be for interfaced systems in which the band gaps of the semiconductors are staggered, with the subsequent improvement of charge carrier separation [12]. Enhanced photocatalytic performance arises from the fact that photo-generated charge carriers are stabilized on two different semiconductors, achieving limited electron–hole pair recombination. The formation of a direct Z-scheme or S-scheme heterojunction flanking two semiconductors without electron mediators was proposed by Prof. Yu quite recently [13]. Among all of the materials proposed, g-C_3N_4, derived by the direct heating of a cyanamide precursor in air at different temperatures, has risen in importance thanks to the high production of H_2 from the water photo-splitting process upon visible light irradiation. However, despite the undoubted promising properties characterizing the promising photocatalyst exhibited by g-C_3N_4, some drawbacks have limited its practical application: the high electron–hole recombination rate, low quantum and separation efficiencies and the small specific surface area, resulting in large nanoparticles, dramatically affect its photocatalytic performance. For this reason, g-C_3N_4 has been coupled with other semiconductors, such as TiO_2, ZnO and WO_3, forming the direct heterojunction Z-scheme, obtaining very promising results [14–18].

In this preliminary work, we explored different synthesis processes for the preparation of mixed systems of C_3N_4/ZnO. The goal was to tune a facile, cheap and green synthesis process for the preparation of a mixed photocatalyst for oxidation and reduction reactions. We used different precursors and different approaches. We characterized the obtained materials via structural, optical and morphological analyses.

2. Results and Discussion

2.1. Structural Characterization of Supramolecular Precursors

Figure 1 reports the X ray Powder Diffraction (XRPD) patterns of supramolecular complexes (CMW and CME) and pure melamine (M). The supramolecular complexes were prepared by mixing melamine and cyanuric acid in either a water (CMW) or ethanol (CME) environment. The samples were dried in the oven at 70 °C for two days. Melamine was used as received. Indeed, before moving on to the discussion about the structural, morphological and optical features characterizing and differentiating the synthetized samples, it is worth evaluating the structural properties of the prepared precursors for subsequent C_3N_4 production. Accordingly, both of the new molecular arrangements exhibited by the supramolecular structural patterns show reflections at 10.67°, 18.48° and 21.41° 2θ values, indexed as (100), (100) and (200), respectively, in previous papers [19–22]. These low-angle reflections are considered evidence of the in-plane hexagonal channel structure within this supramolecular structure. Moreover, Ref. [23] attributed the higher-angle reflection present at 2θ values of 27.9° characterized by higher intensity to a d-spacing of about 0.320 nm, compatible with a graphite-like stacking of individual 2D sheets. The same evidence should be revealed by the reflection at 29.75°, in particular, for the (002) family plane, as proposed by Shalom et al. [19]. Finally, it is possible to note that the intensity of the two patterns differs a bit when changing the reaction environment, with the supramolecular structure grown in water (CMW) slightly more intense than the one in ethanol (CME): this could also be an indication of the different morphologies of the two synthetized precursors due to an altered growth path dictated by the solvent.
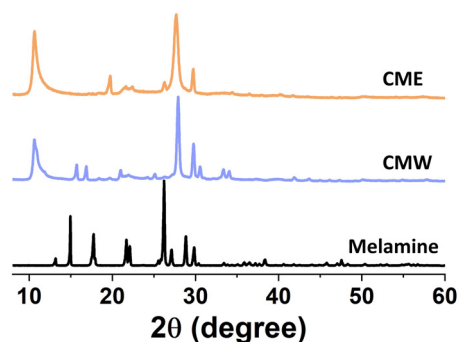
Figure 1. XRPD (X ray Powder Diffraction) pattern of the supramolecular structures synthetized starting from a mixture of melamine and cyanuric acid in water (CMW, light-blue line) and ethanol (CME, yellow line) and XRPD pattern of pure melamine.

2.2. Characterization of Bare C_3N_4

As described in Section 3.1.2, bare C_3N_4 batches were synthetized both by the direct thermal condensation of melamine (at 550 °C for 4 h in air, C_3N_4-M) and by thermal polycondensation of the previously prepared melamine–cyanuric acid supramolecular complexes, CMW (C_3N_4-CMW) and CME (C_3N_4-CME). Figure 2a reveals that the C_3N_4-M sample displays the typical XRD fingerprint of carbon nitride materials, namely, the presence of an intense reflection around a 27° 2θ angle, corresponding to an inter-planar distance of almost 0.326 nm and considered a peculiar feature associated with the (002) plane of two-dimensional aromatic systems in graphite-like structures [24,25]. However, it should be considered that the typical lamellar structure of C_3N_4 is significantly denser than graphene layers in crystalline graphite; this higher density of aromatic system stacking can be attributed to easier electron localization, which would result in a stronger interaction between the superimposed planes [26]. This attribution is confirmed by the pronounced broadening of this reflection, suggesting that overlapping only involves a limited number of layers [27]. Analyzing the pattern, an additional weaker and broader reflection at approximately 13.2° is also noticeable and associated with the (100) plane, indicating the structural periodicity within the individual two-dimensional layers: in particular, this reveals the alternating of tri-s-triazine or s-heptazine repetition units.
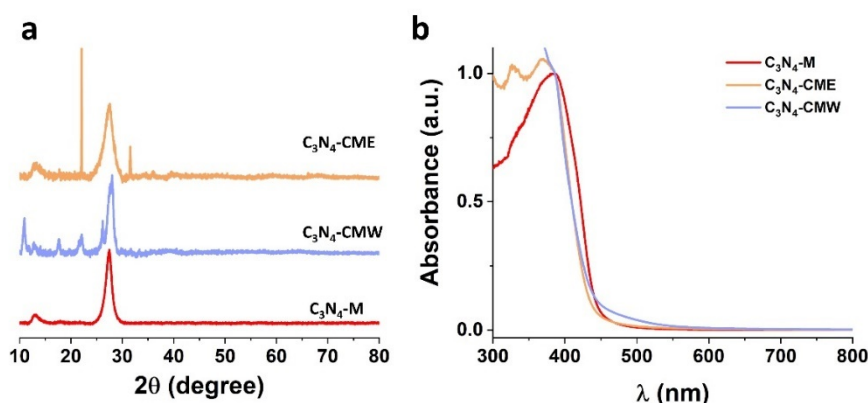
Figure 2. (**a**) XRPD pattern and (**b**) DRS-UV spectra of bare C_3N_4-M samples (red line), C_3N_4-CMW (light-blue line) and C_3N_4-CME (yellow line).

The described reflections are also visible in the patterns of C_3N_4-CMW and C_3N_4-CME samples, where additional signals are present, evidencing impurities in the final material arising from the melamine–cyanuric acid supramolecular complex. Thus, the sample synthetized by melamine thermal condensation shows a higher purity. However, all of the materials are characterized by the same degree of crystallinity. In this regard, C_3N_4-CME

and C_3N_4-CMW seem to have a much broader reflection at higher angles (27°) than C_3N_4-M, suggesting a porous structure in these materials induced by the supramolecular precursor. As reported in Table 1, the surface areas of the prepared materials C_3N_4-CME, C_3N_4-CMW and C_3N_4-M obtained with the BET method are respectively 32, 33 and 11 m^2/g.

Table 1. Summary of the synthetic routes, precursors and thermal treatments employed for the sample preparation. M: melamine ($C_3H_6N_6$); C: cyanuric acid ($C_3H_3N_3O_3$); EtOH: ethanol (CH_3CH_2OH). The energy gaps were evaluated from the Tauc plot (see Section 3.2); the instrumental error is specified as ±0.05 eV.

Sample	Abbreviation	Synthetic procedure	Precursors	Supramol. Complexes	Hydroth. Step	Calcin. Step	Energy Gap (eV)	Surf. Area BET m^2/g
ZnO	ZnO_H	Hydrothermal	$Zn(NO_3)_2$		175 °C for 16 h		3.27	<10
C_3N_4	C_3N_4 –M	Thermal condensation	M			550 °C for 4 h	2.87	~11
C_3N_4	C_3N_4 - CME	Thermal polycondensation	M, C, EtOH (M-C molar ratio 1:1)	X		550 °C for 4 h	3.01	~32
C_3N_4	C_3N_4 - CMW	Thermal polycondensation	M, C, H_2O (M-C molar ratio 1:1)	X		550 °C for 4 h	3.04	~33
ZnO-C_3N_4	ZnO-CME	Thermal polycondensation	$Zn(NO_3)_2$, M, C, EtOH (M-C molar ratio 1:1)	X		550 °C for 4 h	3.20	<10
ZnO-C_3N_4	ZnO-CMW	Thermal polycondensation	$Zn(NO_3)_2$, M, C, H_2O (M-C molar ratio 1:1)	X		550 °C for 4 h	3.19	<10
ZnO-C_3N_4	ZnO-CMW_H	Thermal polycondensation + Hydrothermal	$Zn(NO_3)_2$, M, C, H_2O (M-C molar ratio 1:1)	X	175 °C for 16 h (after first calcination step)	550 °C for 4 h		<10
ZnO-C_3N_4	ZnO-M	Thermal condensation	$Zn(NO_3)_2$, M, EtOH			550 °C for 4 h	3.19	~12
ZnO_H-C_3N_4	DEP 31	Deposition	ZnO_H, M, H_2O (ZnO_H-C molar ratio 3:1)			550 °C for 4 h	3.21	<10
ZnO_H-C_3N_4	DEP 21	Deposition	ZnO_H, M, H_2O (ZnO_H-M molar ratio 2:1)			550 °C for 4 h	3.21	<10
ZnO_H-C_3N_4	DEP 21_H	Deposition	ZnO_H, M, H_2O (ZnO_H-M molar ratio 2:1)		175 °C for 16 h (after first calcination step)	550 °C for 4 h	3.21	<10
ZnO_H-C_3N_4	DEP 11	Deposition	ZnO_H, M, H_2O (ZnO_H-M molar ratio 1:1)			550 °C for 4 h	3.21	<10
ZnO_H-C_3N_4	DEP 11_H	Deposition	ZnO_H, M, H_2O (ZnO_H-M molar ratio 1:1)		175 °C for 16 h (after first calcination step)	550 °C for 4 h	3.21	<10
ZnO_H - C_3N_4	US 31	Ultrasonic/ mechanical mixture	ZnO-H, C_3N_4–M, H_2O (ZnO_H-C_3N_4–M molar ratio 3:1)				3.20	<10
ZnO_H-C_3N_4	US 21	Ultrasonic/ mechanical mixture	ZnO-H, C_3N_4–M, H_2O (ZnO_H- C_3N_4–M molar ratio 2:1)				3.20	<10

In terms of optical spectroscopy, whose spectra are reported in Figure 2b, it can be observed that a qualitative evaluation of the various absorbances does not evidence any significant variation from one sample to the other. The electronic transition from the valence band, mainly constituted by nitrogen p_z orbitals, to the conduction band, made up of carbon p_z orbitals, can be highlighted; this excitation is predominantly promoted by the wavelength around 460 nm and corresponds to an energy value of almost 2.8 eV, in line with previous works [28–32]. However, considering the band gap values obtained by the Tauc plot application, it is possible to see some differences: indeed, we obtained 2.87 eV for C_3N_4-M and 3 eV for C_3N_4-CMW and C_3N_4-CME (Table 1). Considering this result, as evidenced by X-ray analysis, the higher porosity of the suggested structure for the material synthetized by the supramolecular complex, and thus the more extended tri-s-triazine units conjugate system of the C_3N_4, may be the origin of the higher band gap value. Finally, the

slightly longer absorption extension in the visible range for C_3N_4-CMW may be due to the higher presence of impurities in the unreacted supramolecular structure.

2.3. Characterization of C_3N_4-ZnO Heterojunction Synthetized by Prepared Supramolecular Complexes

As described in Section 3.1.3, different synthetic approaches were adopted for the preparation of the double-phase C_3N_4-ZnO heterostructure; the aim was to understand the different structural and optical features that a given synthetic route can lead to in the final material. All of the mixed ZnO-C_3N_4 samples obtained with different synthesis processes present the surface area of pure ZnO_H, about 10 m^2/g, which means that the presence of C_3N_4 does not affect the structure of the bare oxide.

Figure 3a reports the XRPD patterns of the C_3N_4-ZnO heterojunction formed by the simultaneous growth of the phases in the final calcination step (550 °C for 4 h) in air; as described in Table 1, pristine ZnO (used as a benchmark in this study) was produced via hydrothermal synthesis; the heterostructured samples labeled ZnO-CMW and ZnO-CME were obtained using the prepared supramolecular complexes as precursors for the carbon nitride phase, while the sample labeled ZnO-M used C_3N_4 as a precursor in the thermal condensation of melamine. As is observable, except for ZnO-CME, the prepared materials' XRPD patterns are dominated by the typical reflections of ZnO corresponding to the (100), (002), (101), (102), (110), (103), (200), (112), (201), (004) and (104) planes, attributable to the typical wurtzite hexagonal crystal phase (JCPDS 36-1451) [33]; the reflection sharpness confirms the purity and high crystallinity of this phase. Conversely, for the ZnO-CME sample, the ZnO phase reflections are not so intense: only the reflection around the 32° 2θ angle is of appreciable intensity, indicating that the preferential orientation for the nanostructure produced in this sample is probably caused by the nature of the supramolecular complex. However, ZnO-CME and ZnO-CMW are characterized by additional reflections due to impurities caused by unreacted supramolecular reagents, as similarly described in Section 2.2 for the bare C_3N_4. It should be noted that no appreciable signals ascribable to C_3N_4 were observed due to the very low intensity of these reflections.

In an attempt to avoid the observed impurities induced by the unreacted supramolecular complexes, we introduced a hydrothermal step (175 °C for 16 h) before the final calcination treatment in air for the ZnO-CMW sample, now named ZnO-CMW_H. Correspondingly, in the XRPD pattern of hydrothermally treated ZnO-CMW_H, the reflections for the impurities disappeared, and only those related to the ZnO phase are identifiable. Accordingly, hydrothermal treatment by means of the high pressure employed is able to stabilize the organic complex, promoting the complexation of melamine and cyanuric acid in an ordered arrangement of the two monomers, now held together by a greater number of hydrogen bonds and allowing for the net stabilization of the structure [34].

An additional general feature can be derived by analyzing these patterns: the different relative ratio intensities of the three main reflections of ZnO phases (between 2θ values of 30° and 40°) in the sample grown simultaneously to the carbon nitrate phase compared to pristine ZnO are a clear indication of a certain preferential growth direction for ZnO in the presence of the extra phase, where the nature of the precursor of the latter also induces a guiding effect, tailoring the nanoparticle geometry and aspect ratio.
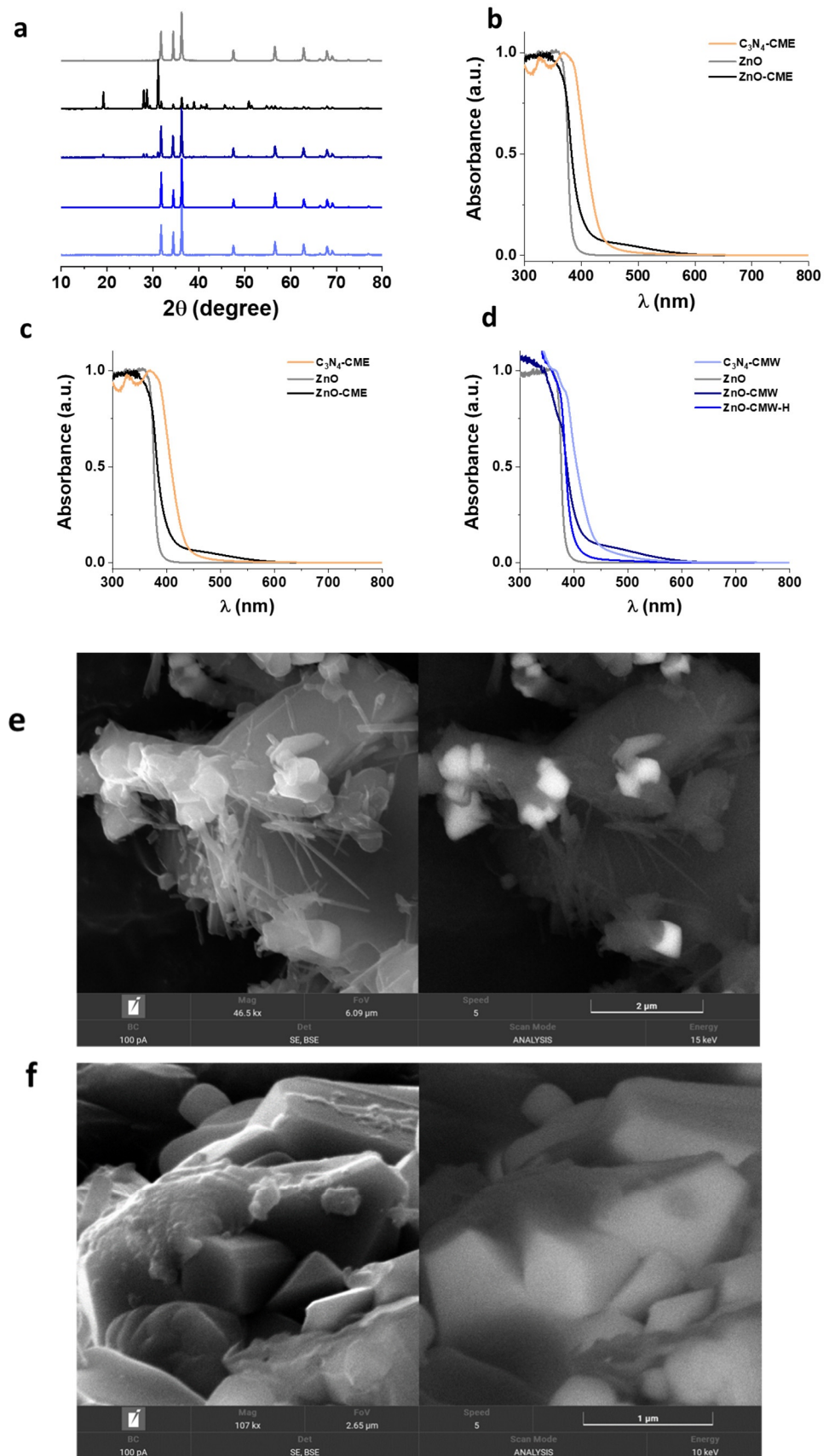
Figure 3. (**a**) XRPD pattern, (**b**–**d**) DRS-UV spectra and FESEM images (secondary electrons on the left and backscattered electrons on the right) of (**e**) ZnO-CME and (**f**) ZnO-CMW heterojunctions.

The absence of C_3N_4 crystallographic peaks in the combined samples is due to different reasons: first, the very low mass of C and N nuclei, and second, the formation of needles or, in some cases, of thin sheets that do not allow the formation of a periodic structure detectable by XRD. Moreover, in support of this suggestion, FESEM images reported in Figure 3e,f highlight the morphological differences in the ZnO-CMW and ZnO-CME samples for both the ZnO and C_3N_4 phases of the mixed materials: while ZnO-CME is composed of large hexagonal base shaped ZnO nanorods decorated by C_3N_4 nanoneedles, ZnO-CMW is characterized by narrower nanorods, with a smaller hexagonal base shape, embedded in the C_3N_4 matrix, thus providing a higher interaction area between the two phases. Moreover, the morphological differences between the two samples may suggest that water allows stronger mixing with the reagent and more intimate contact between the two phases.

However, in contrast to other papers [15,35,36], the crystallinity of the ZnO phase is not degraded in the final heterojunction; inter alia, the reflections for ZnO in the mixed materials remain as high and sharp as those for pristine ZnO. Furthermore, FESEM images also agree with this assumption, as already discussed.

While XRPD analysis does not evidence the presence of C_3N_4, DRS UV-vis spectroscopy shows features attributable to the carbon nitride phase, as observable in Figure 3b–d. Generally, all of the mixed C_3N_4-ZnO materials exhibit an intermediate behavior between the two constituting phases: this is deducible by the energy gap values calculated with the Tauc plot and reported in Table 1, displaying a visible red-shift relative to ZnO optical absorption. The visible photon absorption improvement in the case of the heterojunctions is attributable to the presence of the nitride, suggesting the strong cooperation of the two phases at the interface. Moreover, the absorption tail in the mixed samples around 500 nm, which is not present in the bare C_3N_4 samples, may be attributed to the higher defectiveness of this phase in the mixed system as a result of simultaneous crystallization with the ZnO phase during C_3N_4 condensation, as already discussed in previous research [15,35,37–39]: this seems to be particularly important for the more defective materials, such as ZnO-CMW, ZnO-CME and ZnO-M. This effect decreases for the thermally treated ZnO-CMW_H, probably due to the higher sintering process of the two phases and the loss of many intimate contacts among them. Then, it can be confirmed that the simultaneous growth of the two phases from different precursors and their contemporary existence are beneficial in terms of the wider range of photons absorbed compared to the bare materials in both the UV and visible ranges, revealing intimate cooperation during light absorption, determined by a successful charge carrier transfer at the interfaces. Photoactivity measurements such as EPR (electron paramagnetic resonance) experiments under light irradiation will be necessary to confirm this behavior [15]. Furthermore, the formation of the heterojunction will be demonstrated via photocurrent experiments [40–42].

2.4. Characterization of C_3N_4-ZnO Heterojunction Synthetized by Deposition Method

The C_3N_4-ZnO heterojunction was also prepared by applying a deposition method, as described in Section 3.1.5. We attempted to let melamine condensate and polymerize in the presence of the already-formed ZnO nanoparticles (ZnO_H), thus trying to realize C_3N_4 film growth on the ZnO surface. Referring to the results presented in the previous section and, in particular, to the FESEM images, we observed that the water medium could potentially allow establishing more extended surface contact between the two components of the heterojunction (as for ZnO-CMW). Therefore, deposition of C_3N_4 was performed by mixing melamine and ZnO in H_2O; this series of samples is named DEP followed by the indication of the ZnO/melamine molar ratio, thus obtaining DEP 31, DEP 21 and DEP 11 (see Table 1). Evaluating the XRPD analysis results for this set of samples in Figure 4a, one can realize that only DEP 31 shows the typical fingerprints of ZnO, as described in Section 2.3; indeed, the DEP 21 and DEP 11 patterns are studded by many reflections that are attributable to neither the ZnO phase nor the C_3N_4 phase. For this reason, such samples were subjected to a second calcination step, in which the impurities

were completely eliminated, as appreciable in the extension of Figure 4a. Then, it emerges that, depending on the relative concentration of the melamine precursors, the final material shows a different purity degree, requiring longer thermal treatment: it could be that, in the presence of too high an amount of organic precursor, the surface sites of ZnO nanoparticles from which the C_3N_4 phase nucleates are completely occupied, leaving the excess precursor unreacted. This consideration is also supported by FESEM images of sample DEP 31, visible in Figure 4c: the ZnO nanorods, hardly recognizable by the hexagonal base shape, are submerged in an environment of C_3N_4 lamellar nanoparticles, appearing much more crystalline when compared to the ones derived from the supramolecular complexes (see FESEM images in Figure 3e,f).
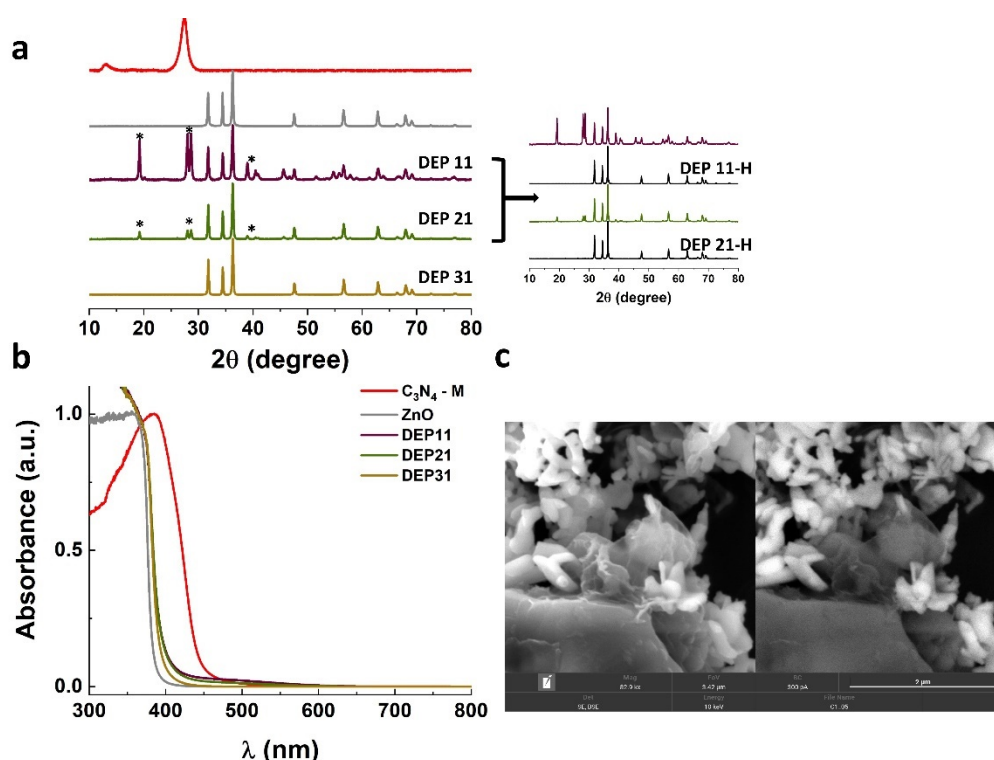

Figure 4. (**a**) XRPD pattern (in the extended part, the diffractograms of the DEP 11 and DEP 21 samples before and after (DEP 11-H and DEP 21-H) the second hydrothermal treatment are reported), (**b**) DRS-UV spectra and (**c**) FESEM images (secondary electrons on the left and backscattered electrons on the right) of DEP 31 heterojunction.

From an optical point of view, the three materials exhibit similar behavior, with an appreciable red-shift absorption edge when compared to pristine ZnO, but less pronounced relative to that observed in the heterostructures prepared through the supramolecular precursor (Section 2.3). In this case, the higher visible light absorption tail (around 500 nm) was recorded for DEP 11, indicating better cooperation between the oxide and nitride phases after the second calcination step. In addition, this reveals that for the deposition synthesis route, the identification of an optimal reaction time that strictly depends on the amount of the organic precursor is crucial in order to obtain the desired performance in terms of visible light harvesting exploited by the heterojunction.

2.5. Characterization of C_3N_4-ZnO Heterojunction Synthetized by Ultrasonic/Mechanical Method

Several studies have reported liquid exfoliation as an effective top-down method to obtain thin layers of C3N4 starting from the bulk material [36,43,44]. Such preparation can easily be obtained through the sonication of C_3N_4 dispersed in a medium. Therefore, as a further alternative procedure, the ZnO/C_3N_4 heterojunction was synthetized through the mechanical mixture of C_3N_4 and ZnO, both synthetized independently and treated with

ultrasounds, with the purpose of making exfoliated C_3N_4 sheets to deposit on the ZnO surface (US samples, see Table 1). Again, since water was observed to be a good dispersal medium in terms of the homogeneous dispersion of the starting materials, we proceeded with the suspension of two previously prepared phases in an aqueous environment. The bulky starting materials ZnO and C_3N_4 synthetized via hydrothermal and melamine condensation were each used for mechanical mixing.

XRPD characterization in Figure 5a reveals typical patterns for the two bare materials employed in ultrasonic mixing and the materials obtained from them, designated US 21 and US 31: a great difference from the XRPD patterns of the other mixed samples reported in the previous sections immediately emerges, namely, the appearance of the reflection at the 27° 2θ angle for the C_3N_4 matrix. This may indicate that with this synthetic route, the nitride phase can maintain a higher crystallinity degree: this would overcome one of the most challenging issues concerning the employment of C_3N_4 in photocatalysis, that is, rapid charge carrier recombination, mainly due to the low surface area and the high amorphization degree. Indeed, in more crystalline materials, thanks to the long-range order, the photoinduced charge carrier pairs have much more time to travel in the solid, thus preventing their recombination. According to Cao et al., light absorption of semiconductor materials is primarily controlled by the band gap, which in turn can be tuned by changing morphology, crystalline quality and crystal structure. A post-annealing treatment can be used as a method to improve the crystallinity and thus the light absorption of semiconductor materials [45]; moreover, the interlayer region generated by the coupling of the two composites may reduce electron–hole recombination [46]. Conversely, this structural advantage is not exhibited by the DRS UV-vis spectroscopy results in Figure 5b, where an appreciable band gap red-shift is not detected, in contrast to the previous cases, with values around 3.20 eV. This behavior is more evident in the material with lower nitride content. Moreover, no additional shoulders arising from C3N4-induced defects during simultaneous growth with ZnO were detected around 500 nm: this can be considered a further indication of the less intimate contact during the solid-state reaction. In this case, the morphology was also explored, with the FESEM image of sample US 31 reported in Figure 5c. The picture reveals the almost complete cleavage of the hexagonal morphology of the starting ZnO_H material (compare with Figure 3e,f), resulting in a lamellar morphology, thus revealing a drastic effect of ultrasonic irradiation on the particle nanostructures. Surprisingly, the C3N4 phase is not easily visible as in the previous synthetized samples: only the backscattered electron image lets us observe its distribution over ZnO platelets by means of darker spots.
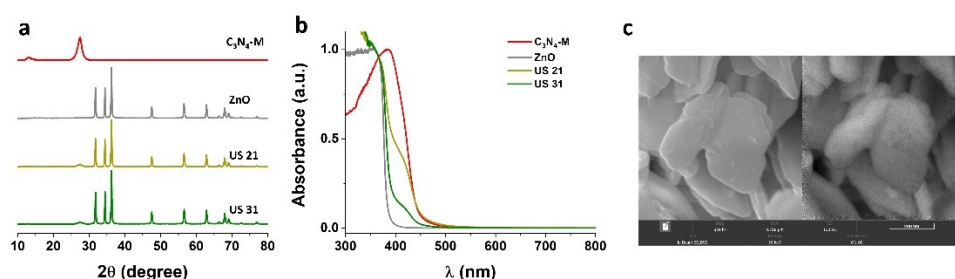

Figure 5. (**a**) XRPD pattern, (**b**) DRS-UV spectra of ZnO, C_3N_4-M, US 31 and US 21 samples and (**c**) FESEM images (secondary electrons on the left and backscattered electrons on the right) of the US 31 heterojunction.

Summarizing, the mechanical mixing achieved via ultrasound irradiation effectively leads to a more crystalline heterojunction characterized by lower visible light harvesting, deriving from the minor cooperation of the two phases at the interface.

3. Materials and Methods

3.1. Sample Preparation

All organic and inorganic reagents employed in the synthesis of the materials were purchased from Sigma-Aldrich and used without any further purification.

The various materials prepared in this work, the different precursors and the synthetic routes employed are summarized in Table 1 (see below).

3.1.1. Bare C_3N_4

Three different bare C_3N_4 samples were synthetized according to the most common procedure, namely, the thermal condensation of the employed precursors, i.e., melamine ($C_3H_6N_6$) and cyanuric acid ($C_3H_3N_3O_3$). Specifically, the material denoted as C_3N_4-M was prepared by the thermal condensation of melamine only (0.977 g) by directly heating the precursor in air at 550 °C for 4 h (5 °C/min ramp). Conversely, two additional pure C_3N_4 materials were produced by developing a supramolecular structure via thermal polycondensation of melamine (0.977 g) and cyanuric acid (1.023 g) dispersed in either H_2O or CH_3CH_2OH: in both cases, the two reagents (in 1:1 molar ratio) were introduced into 80 mL of the respective solvent. The obtained samples were collected and washed (with either water or ethanol, depending on the solvent employed) and dried at 70 °C for two days in the oven; the final materials were obtained by applying a calcination step at 550 °C for 4 h (5 °C/min ramp) and labeled C_3N_4-CMW (water) and C_3N_4-CME (ethanol), respectively.

3.1.2. Bare ZnO

Pristine zinc oxide was synthetized through a hydrothermal procedure, as described in Ref. [47]. Briefly, a 20 mL $Zn(NO_3)_2$ 1M water solution was prepared; following the complete dissolution of the zinc salt, a 4M NaOH solution was added drop by drop to the initial solution until a pH of 11-12 was reached and a dense white precipitate, namely, $Zn(OH)_2$, was visible. Then, the precipitate was inserted into a stainless steel autoclave and treated at 175 °C for 16 h. The obtained ZnO was washed with water and collected by means of centrifugation; finally, the material was dried overnight at 70 °C.

3.1.3. C_3N_4–ZnO Heterojunctions

Inspired by our expertise in the synthesis of transition metal oxide-based semiconductors' photoactive heterojunctions [15,47–49], three different synthetic strategies were employed for the preparation of interfaced C_3N_4-ZnO material, as listed hereafter.

3.1.4. Co-synthesis from Supramolecular Adduct

As described in Section 3.1.1, melamine and cyanuric acid were mixed in either H_2O or CH_3CH_2OH to form the supramolecular adduct to finally obtain C_3N_4 (C_3N_4–CMW and C_3N_4–CME, respectively); in this case, $Zn(NO_3)_2$ (in 1:1:1 molar ratio) was added to the suspension. Once the dissolution of zinc nitrate was completed, a 4M NaOH solution was added dropwise to allow for $Zn(OH)_2$ precipitation. The mixtures were then centrifuged, washed three times with H_2O, dried in the oven at 70 °C, transferred to a crucible and calcined in air at 550 °C for 4 h (5 °C/min ramp). The materials were labeled ZnO-CMW (in water) and ZnO-CME (in ethanol), respectively. An additional sample was realized following the same procedure but starting from melamine and zinc nitrate precursors: this was labeled ZnO-M.

A further modification of this recipe was applied for the material labeled ZnO-CMW_H: it was obtained as described for ZnO-CMW in this section, but before the calcination step in air, the sample was hydrothermally treated in a stainless steel autoclave at 175 °C for 16 h. The sample was then washed with water and collected by means of centrifugation; finally, the material was dried overnight at 70 °C.

3.1.5. Deposition Synthesis

With the aim to allow for the direct polymerization of melamine onto the ZnO-H particle surface, the deposition approach was considered for the preparation of another set of samples with interconnected C_3N_4-ZnO phases. The procedure involved the introduction of melamine to the ZnO-H nanoparticle water suspension; after 30 min of stirring, the samples were dried at 70 °C in the oven for 2 days and eventually calcined at 550 °C for 4 h (5 °C/min ramp). The explored ZnO–melamine molar ratios were 1:1, 2:1 and 3:1, with the obtained samples named DEP 11 (1.56 g of melamine and 1.00 g of ZnO-H), DEP21 (0.76 g of melamine and 1.00 g of ZnO-H) and DEP31 (0.5 g of melamine and 1.00 g of ZnO-H), respectively.

In this case, a further hydrothermal treatment step (175 °C for 16 h) was employed for the DEP11 and DEP21 samples and newly labeled DEP11_H and DEP21_H, respectively.

3.1.6. Ultrasonic/Mechanical Mixture

The last considered synthetic route evaluated the effect of the ultrasonic/mechanical mixture in the constitution of the C_3N_4-ZnO heterojunction. For this procedure, the independently prepared C_3N_4-M and ZnO-H (see Table 1 and Section 3.1.1 and 3.1.2) were dispersed in water with ZnO–C_3N_4 weight ratios of 3:1 and 2:1 and with the corresponding samples referred to as US 31 (0.40 g of melamine) and US 21 (0.55 g of melamine), respectively. The two-phase dispersion was stirred in an ice bath with an immersion sonicator (Bandelin Sonopuls HD 3100 (2022 Merck KGaA, Darmstadt, Germany) equipped with an MS 73 probe, 1 Hz frequency, 30 W power) for 10 min, then centrifuged and dried in the oven at 70 °C for two days.

3.2. Sample Characterization

XRPD (X-ray powder diffraction) was performed to obtain structural information regarding single- and multiple-phase synthetized materials, paying particular attention both to the phase identification and to the possible presence of additional impurity reflections, especially arising from the organic precursors. The acquired patterns were recorded by means of a PANalytical PW3040/60 X'Pert PRO MPD (Malvern Panalytical Ltd., Malvern, UK) with a copper K radiation source (0.15418 nm) in Bragg–Brentano geometry. Samples were scanned continuously in the 2θ range between 10° and 80°. The X'Pert High-Score (Malvern Panalytical Ltd, Malvern, UK) software was used to identify the mineral phases present in the samples.

Diffuse Reflectance UV-vis spectroscopy was employed to characterize the samples from an optical point of view; the optical spectra were recorded using a Varian Cary 5000 spectrophotometer (Agilent, Santa Clara, CA, USA) and the Carywin-UV/scan software (Agilent, Santa Clara, CA, USA). A sample of PTFE with 100% reflectance was used as a reference. The optical band gap energies were calculated by applying the Tauc plot on the obtained spectra, considering that the energy dependence of the absorption coefficient for semiconductors in the region near the absorption edge is proportional to the material energy gap and dependent on the kind of transition (direct or indirect allowed) [50].

FESEM (Field-Emission Scanning Electron Microscope) images were recorded with the instrument FEG-SEM TESCAN S9000G (Source: Schottky emitter; Resolution: 0.7 nm at 15 keV (in-beam SE) (Libušina tř. 21, 623 00 Brno–Kohoutovice, Czech Republic); Accelerating Voltage: 0.2–30 keV; Microanalyzer: OXFORD (Abingdon OX13 5QX, UK); Detector: Ultim Max; Software: AZTEC (Casole Bruzio CS, 87059, Italy)

Surface area measurements were carried out on a Micromeritics Accelerated Surface Area and Porosimetry System (ASAP) 2020/2010 (4356 Communications Drive, Norcross, GA 30093, USA) using the Brunauer–Emmett–Teller (BET) equation on the N_2 adsorption measurement. Prior to the adsorption run, all samples were outgassed at 160 °C for 3 h.

4. Conclusions

In this study, we systematically investigated the structural, optical and morphological features arising from the use of different synthetic routes of the C_3N_4-ZnO heterojunction. Specifically, the different applied preparations for the C_3N_4-ZnO heterostructures included:

✓ The production of a supramolecular precursor realized by the dispersion of melamine and cyanuric acid in water or ethanol, subsequently mixed with zinc precursors and thermally calcined. In this case, we demonstrate that the prepared supramolecular complexes show the expected molecular structures. The addition of a further hydrothermal step after the thermal treatment in air was decisive in obtaining a mixed material free from impurities.

✓ Direct growth by means of melamine thermal condensation of C_3N_4 on hydrothermally pre-formed ZnO nanoparticles.

✓ The ultrasonic/mechanical mixing of both pre-formed ZnO (from hydrothermal synthesis) and C_3N_4 (from melamine-only condensation) nanopowders.

✓ A significant trend can be extrapolated from this experimental approach involving the different intimate contacts between the two phases, strictly connected to the particular preparation method adopted: it appears that the heterojunction prepared starting from the supramolecular complex shows a tighter association between the two phases, resulting in much higher visible light harvesting (connected to the appearance of adsorption bands in the visible region); on the other hand, lower crystallinity is observed.

✓ An intermediate situation is represented by the material obtained via the deposition method, where improved crystallinity, especially regarding the nitride phase, is accompanied by less optical activity at visible frequencies.

✓ Finally, solid-state mixing supported by ultrasound irradiation provided crystalline materials with a completely modified morphology compared to the starting nanostructures.

In conclusion, this study provides a useful tool for obtaining C_3N_4-ZnO heterojunctions by different synthetic procedures, characterized by diverse features concerning structural, optical and morphological peculiarities. We are confident that these materials could be employed in photocatalytic applications thanks to the formation of the designed heterojunctions. The final goal will be to overcome charge carrier pair recombination and extend their lifetime.

Conflicts of Interest: The authors declare no conflict of interest.

References

1. Baly, E.C.C.; Heilbron, I.M.; Barker, W.F. CX.—Photocatalysis. Part I. The Synthesis of Formaldehyde and Carbohydrates from Carbon Dioxide and Water. *J. Chem. Soc. Faraday Trans.* **1921**, *119*, 1025–1035. [CrossRef]
2. Hernandez-Ramirez, A.; Medina-Ramirez, I. *Photocatalytic Semiconductors*; Springer International Publisher: Cham, Switzerland, 2016.
3. Coronado, J.M.; Fresno, F.; Hernàndez-Alonso, M.D.; Portela, R. *Design of Advanced Photocatalytic Materials for Energy and Environmental Applications*; Springer: London, UK, 2013.
4. Ollis, D.F.; Pelizzetti, E.; Serpone, N. Destruction of Water Cntaminants. *Environ. Sci. Technol.* **1991**, *25*, 1522–1529. [CrossRef]
5. Hoffman, M.R.; Martin, S.T.; Choi, W.; Bahnemann, D.W. Environmental Applications of Semiconductor Photocatalysis. *Chem. Rev.* **1995**, *95*, 69–96. [CrossRef]
6. Maeda, K.; Domen, K. Photocatalytic Water Splitting: Recent Progress and Future Challenges. *J. Phys. Chem. Lett.* **2010**, *1*, 2655–2661. [CrossRef]
7. Domen, K.; Kondo, J.N.; Michikazu, H.; Tsuyoshi, T. Photo- and Mechano-Catalytic Overall Water Splitting Reactions to Form Hydrogen and Oxygen on Heterogeneous Catalysts. *Bull. Chem. Soc. Jpn.* **2000**, *73*, 1307–1331. [CrossRef]
8. Chang, Z.; Wang, T.; Gong, J. CO_2 photo-reduction: Insights into CO_2 activation and reaction on surfaces of photocatalysts. *Energy Environ. Sci.* **2016**, *9*, 2177–2196. [CrossRef]
9. Inoue, T.; Fujishima, A.; Konishi, S.; Honda, K. Photoelectrocatalytic Reduction of Carbon Dioxide in Aqueous Suspensions of Semiconductor Powders. *Nature* **1979**, *277*, 637–638. [CrossRef]
10. Jerez, S.; Lopez-Romero, J.M.; Turco, M.; Jimenez-Guerrero, P.; Vautard, R.; Montavez, J.P. Impact of Evolving Greenhouse Gas Forcing on the Warming Signal in Regional Climate Model Experiments. *Nat. Commun.* **2018**, *9*, 1304. [CrossRef]
11. Figures, C.; Schellnhuber, H.J.; Whiteman, G.; Rockström, J.; Hobley, A.; Rahmstorf, S. Three Years to Safeguard our Climate. *Nature* **2017**, *546*, 593–595. [CrossRef]
12. Wang, H.; Zhang, L.; Chen, Z.; Hu, J.; Li, S.; Wang, Z.; Liu, J.; Wang, X. Semiconductor Heterojunction Photocatalysts: Design, Construction, and Photocatalytic Performances. *Chem. Soc. Rev.* **2014**, *43*, 5234–5244. [CrossRef] [PubMed]
13. Yu, J.; Wang, S.; Low, J.; Xiao, W. Enhanced Photocatalytic Performance of Direct Z-Scheme g-C_3N_4-TiO_2 Photocatalysts for the Decomposition of Formaldehyde in Air. *Phys. Chem. Chem. Phys.* **2013**, *15*, 16883–16890. [CrossRef] [PubMed]
14. Kong, L.; Zhang, X.; Wang, C.; Xu, J.; Du, X.; Li, L. Ti^{3+} Defect mediated g-C_3N_4/TiO_2 Z-Scheme System for Enhanced Photocatalytic Redox Performance. *Appl. Surf. Sci.* **2018**, *448*, 288–296. [CrossRef]
15. Cerrato, E.; Paganini, M.C. Mechanism of Visible Photon Absorption: Unveiling of the C_3N_4–ZnO Photoactive Interface by means of EPR Spectroscopy. *Mater. Adv.* **2020**, *1*, 2357. [CrossRef]
16. Zhou, J.; Zhang, M.; Zhu, Y. Preparation of Visible Light-driven g-C_3N_4@ZnO Hybrid Photocatalyst via Mechanochemistry. *Phys. Chem. Chem. Phys.* **2014**, *16*, 17627–17633. [CrossRef]
17. Sun, J.-X.; Yuan, J.-P.; Qia, L.-G.; Jiang, X.; Xie, A.-J.; Shen, Y.-H.; Zhu, J.-F. Fabrication of Composite Photocatalyst g-C_3N_4–ZnO and Enhancement of Photocatalytic Activity under Visible Light. *Dalton Trans.* **2012**, *41*, 6756–6763. [CrossRef] [PubMed]
18. Huang, l.; Xu, H.; Li, Y.; Li, H.; Cheng, X.; Xia, J.; Xu, Y.; Cai, G. Visible-Light-induced WO_3/g-C_3N_4 Composites with Enhanced Photocatalytic Activity. *Dalton Trans.* **2013**, *42*, 8606–8616. [CrossRef] [PubMed]
19. Shalom, M.; Inal, S.; Fettkenhauer, C.; Neher, D.; Antonietti, M. Improving Carbon Nitride Photocatalysis by Supramolecular Preorganization of Monomers. *J. Am. Chem. Soc.* **2013**, *135*, 7118–7121. [CrossRef] [PubMed]
20. Shalom, M.; Guttentag, M.; Fettkenhauer, C.; Inal, S.; Neher, D.; Llobet, A.; Antonietti, M. In Situ Formation of Heterojunctions in Modified Graphitic Carbon Nitride: Synthesis and Noble Metal Free Photocatalysis. *Chem. Mater.* **2014**, *26*, 5812–5818. [CrossRef]
21. Wang, Y.; Zhao, S.; Zhang, Y.; Fang, J.; Chen, W.; Yuan, S.; Zhou, Y. Facile Synthesis of Self-Assembled g-C_3N_4 with Abundant Nitrogen Defects for Photocatalytic Hydrogen Evolution. *ACS Sustain. Chem. Eng.* **2018**, *6*, 10200–10210. [CrossRef]
22. Zhao, S.; Zhang, Y.; Zhou, Y.; Wang, Y.; Qiu, K.; Zhang, C.; Fang, J.; Sheng, X. Facile One-sSep Synthesis of Hollow Mesoporous g-C_3N_4 Spheres with Ultrathin Nanosheets for Photoredox Water Splitting. *Carbon* **2018**, *126*, 247–256. [CrossRef]
23. Jun, Y.-S.; Lee, E.Z.; Wang, X.; Hong, W.H.; Stucky, G.D.; Thomas, A. From Melamine-Cyanuric Acid Supramolecular Aggregates to Carbon Nitride Hollow Spheres. *Adv. Funct. Mater.* **2013**, *23*, 3661–3667. [CrossRef]
24. Goettmann, F.; Fischer, A.; Antonietti, M.; Thomas, A. Chemical Synthesis of Mesoporous Carbon Nitrides Using Hard Templates and Their Use as a Metal-Free Catalyst for Friedel–Crafts Reaction of Benzene. *Angew. Chem. Int. Ed. Engl.* **2006**, *45*, 4467–4471. [CrossRef] [PubMed]
25. Liu, J.; Zhang, T.; Wang, Z.; Dawsona, G.; Chen, W.M. Simple Pyrolysis of Urea into Graphitic Carbon Nitride with Recyclable Adsorption and Photocatalytic Activity. *J. Mater. Chem.* **2011**, *21*, 14398. [CrossRef]
26. Thomas, A.; Fischer, A.; Goettmann, F.; Antonietti, M.; Muller, J.-O.; Schlogl, R.; Carlsson, J.M. Graphitic Carbon Nitride Materials: Variation of Structure and Morphology and their Use as Metal-Free Catalysts. *J. Mater. Chem.* **2008**, *18*, 4893–4908. [CrossRef]
27. Inagaki, M.; Tsumura, T.; Kinumoto, T.; Toyoda, M. Graphitic Carbon Nitrides (g-C_3N_4) with Comparative Discussion to Carbon Materials. *Carbon* **2019**, *141*, 580–607. [CrossRef]
28. Alves, I.; Demazeau, G.; Tanguy, B.; Weill, F. On a New Model of the Graphitic Form of C_3N_4. *Solid State Commun.* **2001**, *109*, 697–701. [CrossRef]

29.   Kumar, S.G.; Karthikeyan, S.; Lee, A.F. g-C$_3$N$_4$-based Nanomaterials for Visible Light-Driven Photocatalysis. *Catalysts* **2018**, *8*, 74. [CrossRef]

30.   Wang, X.; Maeda, K.; Thomas, A.; Takanabe, K.; Xin, G.; Carlsson, J.M.; Domen, K.; Antonietti, M. A Metal-Free Polymeric Photocatalyst for Hydrogen Production from Water under Visible Light. *Nat. Mater.* **2009**, *8*, 76–80. [CrossRef]

31.   Xiao, J.; Han, Q.; Cao, H.; Rabeah, J.; Yang, J.; Guo, Z.; Zhou, L.; Xie, Y.; Bruckner, A. Number of Reactive Charge Carriers—A Hidden Linker between Band Structure and Catalytic Performance in Photocatalysts. *ACS Catal.* **2019**, *9*, 8852–8861. [CrossRef]

32.   Huda, M.N.; Turner, J.A. Morphology-dependent optical absorption and conduction properties of photoelectrochemical photocatalysts for H2 production: A case study. *J. Appl. Phys.* **2010**, *107*, 123703. [CrossRef]

33.   Wróbel, J.; Piechota, J. On the structural stability of ZnO phases. *Solid State Commun.* **2008**, *146*, 324–329. [CrossRef]

34.   Fanetti, S.; Citroni, M.; Dziubek, K.; Nobrega, M.M.; Bini, R. The Role of H-bond in the High-Pressure Chemistry of Model Molecules. *J. Phys. Condens. Matter.* **2018**, *30*, 094001. [CrossRef] [PubMed]

35.   Yu, W.; Xu, D.; Peng, T. Enhanced Photocatalytic Activity of g-C$_3$N$_4$ for Selective CO$_2$ Reduction to CH$_3$OH via Facile Coupling of ZnO: A Direct Z-scheme Mechanism. *J. Mater. Chem. A* **2015**, *3*, 19936–19947. [CrossRef]

36.   Chen, Q.; Hou, H.; Zhang, D.; Hu, S.; Min, T.; Liu, B.; Yang, C.; Pu, W.; Hu, J.; Yang, J. Enhanced Visible-Light Driven Photocatalytic Activity of Hybrid ZnO/g-C$_3$N$_4$ by High Performance Ball Milling. *J. Photochem. Photobiol. A Chem.* **2018**, *350*, 1–9. [CrossRef]

37.   Wang, K.; Li, Q.; Liu, B.; Cheng, B.; Ho, W.; Yu, J. Sulfur-doped g-C$_3$N$_4$ with Enhanced Photocatalytic CO$_2$-Reduction Performance. *Appl. Catal. B Environ.* **2015**, *176*, 44–52. [CrossRef]

38.   Zhai, J.; Wang, T.; Wang, C.; Liu, D. UV-Light-Assisted Ethanol Sensing Characteristics of g-C$_3$N$_4$/ZnO Composites at Room Temperature. *Appl. Surf. Sci.* **2018**, *441*, 317–3323. [CrossRef]

39.   Le, S.; Jiang, T.; Li, Y.; Zhao, Q.; Li, Y.; Fang, W.; Gong, M. Highly Efficient Visible-Light-Driven Mesoporous Graphitic Carbon Nitride/ZnO Nanocomposite Photocatalysts. *Appl. Catal. B Environ.* **2017**, *200*, 601–610. [CrossRef]

40.   Cao, Q.; Li, Q.; Pi, Z.; Zhang, J.; Sun, L.W.; Xu, J.; Cao, Y.; Cheng, J.; Bian, Y. Metal-Organic-Framework-Derived Ball-Flower-like Porous Co$_3$O$_4$/Fe$_2$O$_3$ Heterostructure with Enhanced Visible-Light-Driven Photocatalytic Activity. *Nanomaterials* **2022**, *12*, 904. [CrossRef]

41.   Cao, Q.; Hao, S.; Wu, Y.; Pei, K.; You, W.; Che, R. Interfacial Charge Redistribution in Interconnected Network of Ni$_2$P–Co$_2$P Boosting Electrocatalytic Hydrogen Evolution in both Acidic and Alkaline Conditions. *Chem. Eng. J.* **2021**, *424*, 130444. [CrossRef]

42.   Zhu, L.-Y.; Yuan, K.; Yang, J.-G.; Ma, H.-P.; Wang, T.; Ji, X.-M.; Feng, J.-J.; Devi, A.; Lu, H.-L. Fabrication of Heterostructured p-CuO/n-SnO$_2$ Core-Shell Nanowires for Enhanced Sensitive and Selective Formaldehyde Detection. *Sens. Actuators B Chem.* **2019**, *290*, 233–241. [CrossRef]

43.   Zhang, X.; Xie, X.; Wang, H.; Zhang, J.; Pan, B.; Xie, Y. Enhanced Photoresponsive Ultrathin Graphitic-Phase C$_3$N$_4$ Nanosheets for Bioimaging. *J. Am. Chem Soc.* **2013**, *135*, 18–21. [CrossRef] [PubMed]

44.   Yang, S.; Gong, Y.; Zhang, J.; Zhan, L.; Ma, L.; Fang, Z.; Vaiìjtai, R.; Wang, X.; Ajayan, P.M. Exfoliated Graphitic Carbon Nitride Nanosheets as Efficient Catalysts for Hydrogen Evolution Under Visible Light. *Adv. Mater.* **2013**, *25*, 2452–2456. [CrossRef] [PubMed]

45.   Cao, Q.; Yu, J.; Cao, Y.; Delaunay, J.-J.; Che, R. Unusual Effects of Vacuum Annealing on Large-Area Ag$_3$PO$_4$ Microcrystalline Film Photoanode Boosting Cocatalyst- and Scavenger-free Water Splitting. *J. Mater.* **2021**, *7*, 929–939. [CrossRef]

46.   Nocchetti, M.; Pica, M.; Ridolfi, B.; Donnadio, A.; Boccalon, E.; Zampini, G.; Pietrella, D.; Casciola, M. AgCl-ZnAl Layered Double Hydroxides as Catalysts with Enhanced Photodegradation and Antibacterial Activities. *Inorganics* **2019**, *7*, 120. [CrossRef]

47.   Cerrato, E.; Gionco, C.; Paganini, M.C.; Giamello, E.; Albanese, E.; Pacchioni, G. Origin of Visible Light Photoactivity of the CeO$_2$/ZnO Heterojunction. *ACS Appl. Energy Mater.* **2018**, *1*, 4247–4260. [CrossRef]

48.   Cerrato, E.; Zickler, G.A.; Paganini, M.C. The Role of Yb Doped ZnO in the Charge Transfer Process and Stabilization. *J. Alloys Compd.* **2019**, *816*, 152555. [CrossRef]

49.   Paganini, M.C.; Cerrato, E. Photoactive Systems based on Semiconducting Metal Oxides. In *Material Science in Photocatalysis*; Garcıa-Lopez, E.I., Palmisano, L., Eds.; Elsevier: Amsterdam, The Netherlands, 2021; Volume 1, pp. 221–234.

50.   Tauc, J. *The Optical Properties of Solids*; Academic Press: New York, NY, USA, 1966.